

Mode-locked dark pulse Kerr combs in normal-dispersion microresonators

Xiaoxiao Xue¹, Yi Xuan^{1,2}, Yang Liu¹, Pei-Hsun Wang¹, Steven Chen¹, Jian Wang^{1,2}, Dan E. Leaird¹, Minghao Qi^{1,2} and Andrew M. Weiner^{1,2*}

The generation of Kerr frequency combs in a coherently driven nonlinear microresonator is now extensively investigated more generally by the research community as a potentially portable technology for a variety of applications. Here, we report experiments in which dark pulse combs are formed in normal-dispersion microresonators with mode-interaction-assisted excitation, and mode-locking transitions are observed in the normal-dispersion regime. The mode-interaction-aided excitation of dark pulses appears to occur through a deterministic pathway, in sharp contrast to the situation for bright pulses in the anomalous dispersion region. The ability to mode-lock in the normal-dispersion regime increases the freedom in the microresonator design and may make it possible to extend Kerr comb generation into the visible, where material dispersion is likely to dominate.

The dynamics of microresonator frequency combs (Kerr combs) have attracted intense interest since the first demonstration of the method^{1–25}. It has been found that Kerr combs are not always coherent^{11,12} and may be characterized by high intensity noise^{13,14}. Furthermore, the lack of coherence and high intensity noise are generally correlated. Experiments have revealed transitions from low-coherence, high-noise states to highly coherent mode-locked states, accompanied by a sudden drop in comb noise^{14–18}. The mode-locking mechanisms of Kerr combs harbour rich possibilities that differ from those of traditional mode-locked lasers^{26,27} and that remain under exploration. Processes related to the formation of temporal patterns (including solitons) analogous to spatial structures in a coherently driven nonlinear cavity^{28,29} are particularly interesting. Such temporal structures have been observed experimentally only recently, in anomalous dispersion fibre cavities³⁰ and microresonators¹⁷. With reference to Kerr comb generation, ref. 17 reports a method of tuning the pump laser frequency to an effectively red-detuned regime (with the pump laser wavelength longer than the resonant wavelength), which is typically difficult to achieve due to thermal instability³¹. Mode-locking transitions yielding bright soliton-like pulses were observed after passage through a broadband chaotic state¹⁷.

In contrast to bright pulses in the anomalous dispersion region, the experimental demonstration of dark pulses in normal-dispersion microcavities, although predicted by numerical simulations^{24,25}, has proved to be extremely difficult. The first challenge is spontaneous excitation. Although modulational instability (which is required for the growth of primary comb lines from a continuous-wave (c.w.) field with noise) is possible in normal-dispersion resonators with proper laser-resonance detuning^{32–34}, it requires the pump laser frequency be in the effectively red-detuned region, which is generally unstable due to thermal instability³¹ and modulational-instability-induced intracavity power switching³⁵. Moreover, it is difficult to directly characterize dark pulses with conventional ultrafast techniques such as frequency-resolved optical gating or second-order autocorrelation. Although experimental comb spectra have been ascribed to dark pulse action in refs 36 and 37, no corroborating measurements of spectral-phase or

time-domain profiles were reported and an excitation pathway for dark pulse formation was not proposed.

In this Article, we show that dark pulses can be excited with the aid of mode interactions in normal-dispersion microresonators. For the first time, mode-locking transitions related to dark pulse formation are observed in the normal-dispersion regime, and we demonstrate the time-domain characterization of dark pulses by first converting them to bright pulses via line-by-line pulse shaping¹¹ and then performing autocorrelation or cross-correlation measurements. The mode-interaction-aided excitation of dark pulses appears to occur through a deterministic pathway, in sharp contrast to the situation for bright pulses in the anomalous dispersion region, where the number of peaks generated is stochastic due to the pathway through a chaotic state^{17,19}.

Experimental results

The nonlinear microresonator used here is a SiN microring that shows a strong normal dispersion ($\beta_2 = 190.7 \pm 8.4 \text{ ps}^2 \text{ km}^{-1}$, measured using the method reported in ref. 38, with a corresponding D_2 parameter of $-2\pi \times 10 \text{ MHz}^{5,14,17}$; Fig. 1b). In the first example, a Au microheater is also integrated with the SiN microring (Fig. 1a), which can be used to shift the resonance frequencies by means of the thermo-optic effect. The microheater-based thermal-tuning technique gives us an alternative ultrastable way of controlling the pump-resonance detuning in addition to the conventional method of changing only the pump laser frequency.

For comb generation (see set-up in Fig. 1c) we tuned the microresonator by changing the voltage applied to the microheater to match the resonance wavelength with the pump laser wavelength (see Methods). The free spectral range (FSR) of the mode used for comb generation is $\sim 231.3 \text{ GHz}$ and the loaded resonance width is 250 MHz (corresponding to a loaded quality factor (Q_{loaded}) of 7.7×10^5). By optimizing the heater voltage, broadband frequency combs were generated and transitioned to a low-noise state, which generally corresponds to a highly coherent mode-locked state (Fig. 1d,e). The low-noise transition behaviour and the mode-locked state were also verified by measuring the beat note of the comb line with a narrow-linewidth reference laser (Supplementary Section 1).

¹School of Electrical and Computer Engineering, Purdue University, 465 Northwestern Avenue, West Lafayette, Indiana 47907-2035, USA.

²Birk Nanotechnology Center, Purdue University, 1205 West State Street, West Lafayette, Indiana 47907, USA. *e-mail: amw@purdue.edu

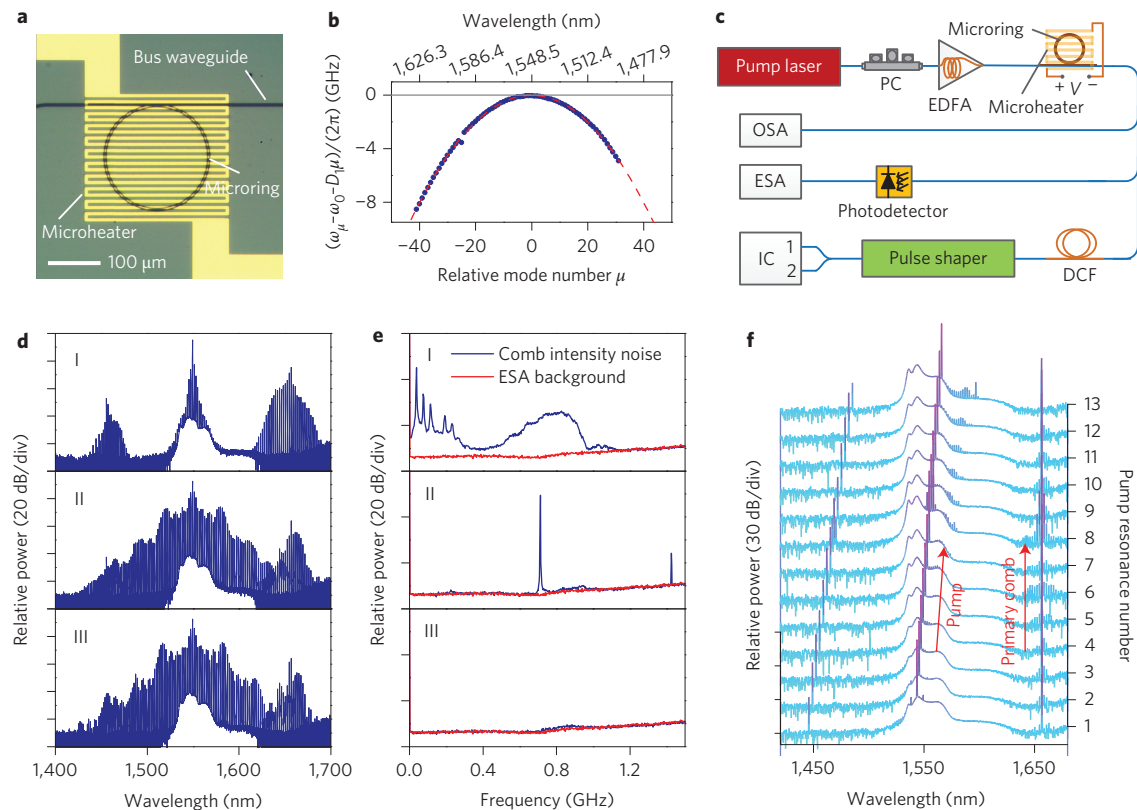


Figure 1 | Comb generation with a normal-dispersion SiN microring. **a**, Microscope image of the microring. **b**, Deviation of the resonance frequencies (blue symbols) $\omega_\mu = \omega_0 + D_1\mu + (1/2)D_2\mu^2 + \dots$ from an equidistant frequency grid defined by $\omega_0 + D_1\mu$ (grey line), where ω_0 is the resonance pumped for comb generation in **d** and μ the relative mode number. $D_1 = 2\pi \times \text{FSR}$, where FSR is the free spectral range at ω_0 . The normal dispersion is described by $D_2 \approx -2\pi \times 10 \text{ MHz}$ (red dashed line; higher-order terms are negligible). **c**, Experimental set-up. PC, polarization controller; EDFA, erbium-doped fibre amplifier; DCF, dispersion-compensating fibre; OSA, optical spectrum analyser; ESA, electrical spectrum analyser; IC, intensity correlator. **d**, Comb generation showing a mode-locking transition. See Methods for descriptions of I, II and III. **e**, Comb intensity noise (resolution bandwidth, 1 MHz). The pump power is injected further into the microring from I, II and to III by controlling the detuning between the pump laser and resonance (see Methods). **f**, Primary comb pinning, which is a signature of mode interaction (see the main text for comb generation details).

Our microresonator-tuning method is equivalent to the traditional method of tuning the pump laser wavelength from the blue side to stably approach the resonance, which is redshifted by thermo-optic and Kerr effects¹⁷. This leads to the intracavity pump field staying on the upper branch of the bistability curve where modulational instability is generally absent^{32–34} (Supplementary Section 3). We believe the initial comb lines shown in Fig. 1d,I were formed due to the interaction of different mode families^{18,39–41}. In overmoded microresonators, mode coupling may occur between different mode families around mode crossing positions. The resonant frequency of each mode is shifted, which may equivalently be viewed as an additional per roundtrip phase shift for each of the corresponding comb frequency components. The phase relationship between the pump mode and the two sideband modes, one of which is coupled to the other transverse mode, may be affected such that an equivalent anomalous dispersion is achieved. Modulational instability thus occurs and generates some initial comb lines. To provide evidence for the mode interaction, we pumped different resonances belonging to the same transverse mode family as that pumped in Fig. 1d. The pump power was reduced to 0.6 W so that only two primary comb lines were generated in the optical spectrum analyser range (Fig. 1f). The pump was shifted by a total of 2.76 THz (12 FSRs), while the long-wavelength sideband varied by no more than $\pm 15 \text{ GHz}$. The short-wavelength sideband varied at twice the rate of pump tuning, for a total variation of 5.52 THz. The long-wavelength sideband was always anchored at the same position, which is a signature of mode-interaction-aided comb generation⁴⁰.

The resonance frequency shifts induced by mode interactions may change when we thermally tune the microresonator, because the thermal tuning rates of the two spatial mode families differ and because the mode coupling coefficient depends on the resonance wavelength⁴⁰. To further investigate the relationship between mode interaction and the broadband comb in Fig. 1d, we shifted the entire mode-locked comb spectrum after transition by tuning the pump laser wavelength and the microresonator in tandem (that is, tuning them, in turn, in small steps of $<0.01 \text{ nm}$). Figure 2a shows the tunable comb spectra measured with the pump wavelength tuned over a total range of 1,549–1,550.4 nm. Except for lines near the mode interaction areas at the edges of the spectral envelope, the amplitude of each comb line remained nearly constant. A low-noise state could be achieved for all the combs by optimizing the laser–microresonator detuning. It can be observed from Fig. 2a that the comb cluster around 1,660 nm, which was mainly attributed to mode interaction, disappeared when the pump laser wavelength was tuned below 1,549.1 nm or above 1,549.6 nm. The comb spectrum thus became more symmetric. The results suggest that the mode interaction became weaker when the microresonator was thermally tuned to match the pump wavelength in these ranges. Our experiments also showed that the broadband comb could not be generated with the pump laser fixed in approximately the same range below 1,549.1 nm or above 1,549.6 nm where the mode interaction induced comb cluster was absent. The broadband comb was preferably generated with the pump fixed in the range above 1,549.1 nm and

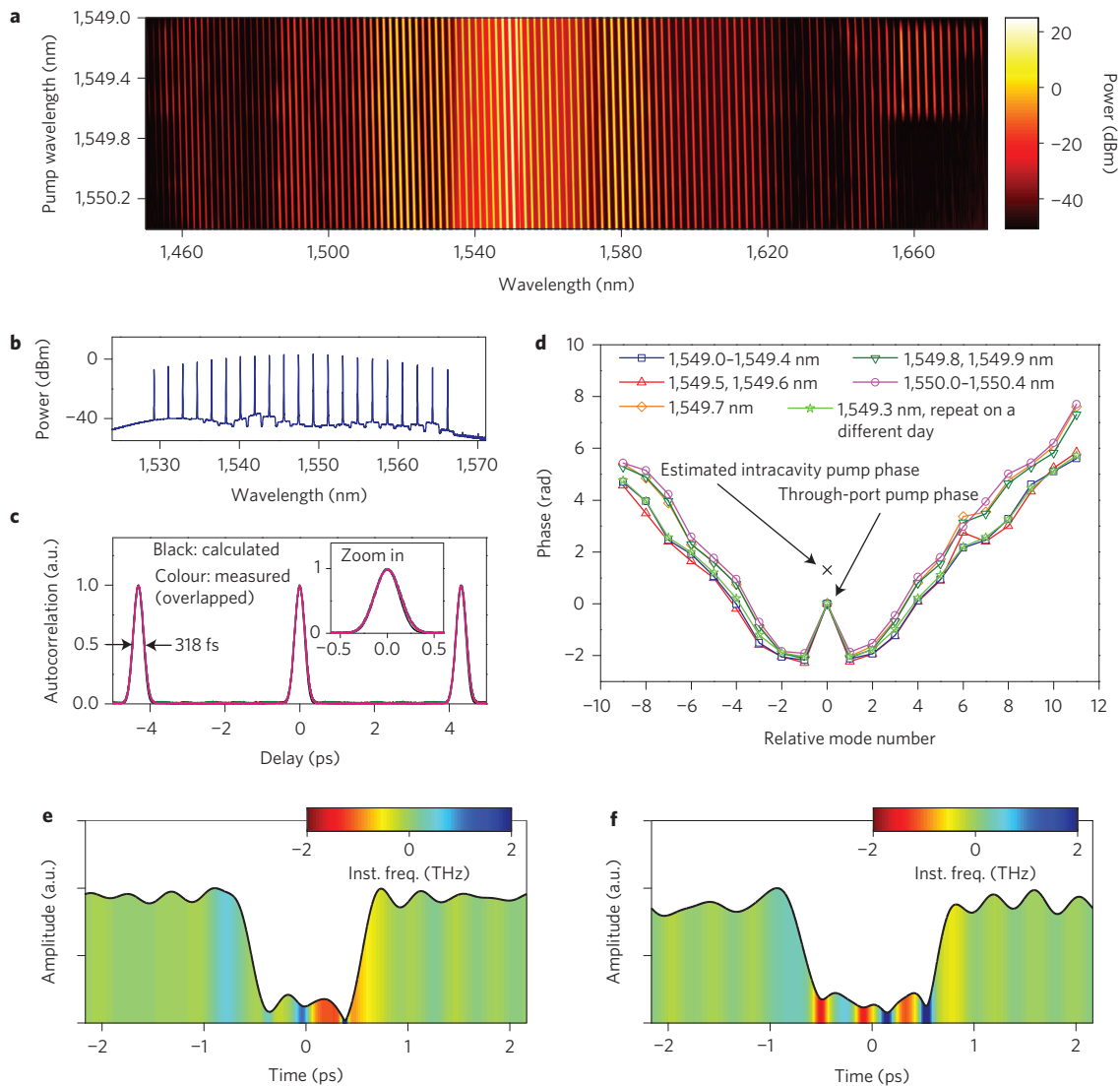


Figure 2 | Comb characterization through line-by-line shaping. **a**, Spectrum tuning of the broadband comb. The comb was initially generated with a pump wavelength of 1,549.3 nm and then tuned between 1,549.0 and 1,550.4 nm in steps of 0.1 nm. **b**, Shaped Gaussian spectrum before the autocorrelator (pumping at 1,549.3 nm). **c**, Measured intensity autocorrelation when the comb phases were compensated to form a transform-limited pulse train. There are 16 overlapping curves. One is the result calculated by assuming perfect compensation, and the other 15 each correspond to individual combs with different pump wavelengths. **d**, Retrieved comb phase using the $\exp(i\omega t)$ sign convention commonly used in ultrafast optics. The different curves correspond to different pump wavelengths. **e, f**, Reconstructed time-domain waveforms in the microresonator with pump wavelengths of 1,549.3 and 1,550.4 nm, respectively. Inst. freq., instantaneous frequency. The comb lines used for reconstruction contain 82% of the total power excluding the pump (91% including the pump).

below 1,549.6 nm, but then might be tuned outside this range. The experimental evidence shows that the broadband comb, although excited by mode interaction induced initial combs, was not governed by the mode interaction. There is another mechanism responsible for the stable broadband comb, which in the following is recognized as dark pulse formation.

We used a pulse shaper in the lightwave C band to perform line-by-line shaping of the mode-locked frequency comb. A total of 21 comb lines fell in the frequency range of the pulse shaper. The spectral shape was tailored (Fig. 2b) and the phase was compensated to form a transform-limited pulse train (see Methods)¹¹. All the combs at different pump wavelengths shown in Fig. 2a could be cleanly compressed, with high contrast, to a duration of ~ 318 fs (autocorrelation width corresponding to ~ 220 fs pulse width; Fig. 2c), indicating that high coherence was maintained. The compressed autocorrelations measured for 15 different combs shifted by 0.1 nm wavelength increments are overlapped and are essentially indistinguishable. The retrieved comb phase curves are shown in

Fig. 2d. A small variation of the phase curve can be observed during the comb tuning process, which coincides with the change in the comb spectrum in Fig. 2a. We attribute this to the change of mode interaction. Nevertheless, the phase curves remain similar. The repeatability of this state of the comb is extremely good. Figure 2d also shows one comb phase curve that was measured on a different day with a pump wavelength of 1,549.3 nm. A result very similar to the other curves was obtained. The ability to maintain a nearly unchanged low-noise state, even while tuning nearly a full FSR and experiencing changes in the mode interactions that initiate the comb, signifies the robust character of the discovered mode-locked operating regime.

By using the spectral phase information (Fig. 2d) retrieved via line-by-line pulse shaping and the power spectrum measured without amplitude shaping, we can reconstruct the time-domain waveform in the microresonator. To do so, the amplitude and phase of the pump line measured at the through port are first corrected to represent the component from coupling out of the

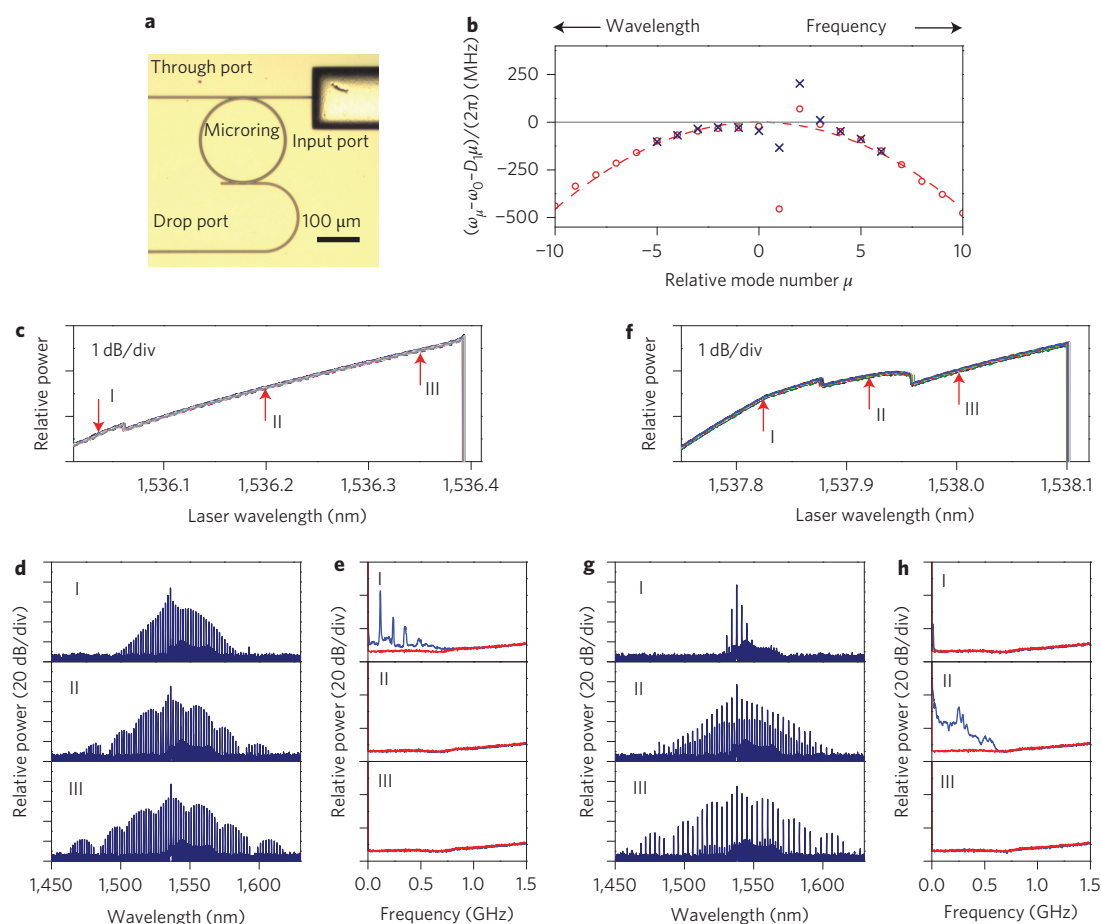


Figure 3 | Drop-port investigation of normal-dispersion combs. **a**, Microscope image of the microring. **b**, Deviation of the resonance frequencies from an equidistant frequency grid. The definitions of $\omega_0 + D\mu$, ω_0 and μ are the same as those in Fig. 1b. Mode 0 corresponds to the resonance around 1,537.4 nm. Red circles, cold cavity; blue crosses, pumped cavity when mode -7 is pumped with ~ 1 W. **c, f**, Drop-port power transmission when mode 1 (**c**) and mode 0 (**f**) are pumped for comb generation. Twenty measurements are closely overlapped with different colours. **d, e**, Comb spectrum and intensity noise (blue) at each stage when mode 1 is pumped. **g, h**, Comb spectrum and intensity noise (blue) at each stage when mode 0 is pumped. The background noise of the electrical spectrum analyser (red) is also shown in **e** and **h**.

microring cavity (see Supplementary Section 4 for a discussion of the analysis procedure and also for corroborating experiments obtained for another resonator fabricated with a drop port). The reconstructed waveforms at different pump wavelengths are shown in Fig. 2e,f, which are square dark pulses with chirped edges and chirped ripples at the bottom. The dark pulses have a complex structure, in sharp contrast to the isolated pulse bright solitons in the anomalous dispersion region (see Supplementary Section 5 for results measured with a larger pulse shaping range).

Figure 3 shows the results of another microring example fabricated with both through port and drop port ($Q_{\text{loaded}} = 8.6 \times 10^5$; ref. 42). The advantage of a drop port is that the intracavity field may be observed without the complication of a strong superimposed pump field. The waveguide constructing the microring (shown in Fig. 3a) has nominally the same dimensions as the one in Fig. 1a, and the measured dispersion ($\beta_2 = 186.9 \pm 7.3 \text{ ps}^2 \text{ km}^{-1}$) matches within experimental error (Fig. 3b). Here, strong mode interactions occur for modes 1 (relative mode number $\mu = 1$) and 2 ($\mu = 2$), which can be concluded from the corresponding resonance jumps in Fig. 3b. For comb generation, the pump laser frequency was tuned slowly into resonance from the blue side. The pump power was ~ 1 W. In two tests, modes 1 and 0 were pumped, generating 1-FSR and 2-FSR combs, respectively. Figure 3c,f shows the optical power transmission measured at the drop port when the pump laser was scanned across the resonance from the blue side

(scanning speed of 0.5 nm s^{-1}). Similar to the case of bright soliton formation in the anomalous dispersion region¹⁷, power drop steps that indicate transition behaviour can be observed here. It has been shown that the power drop steps related to bright soliton formation randomly change from scan to scan, which implies a stochastic transition pathway¹⁷. In contrast, in Fig. 3c,f, where 20 measurements under repeated laser scans are overlaid, the traces are virtually identical, providing evidence for a deterministic pathway toward mode-locking in the normal-dispersion region. The comb spectra and intensity noise at different stages are shown in Fig. 3d,e (for the 1-FSR comb) and Fig. 3g,h (for the 2-FSR comb). A low-noise mode-locking transition was observed in both cases.

The 1-FSR and 2-FSR mode-locked combs shown in Fig. 3d,III and Fig. 3g,III, respectively, have a similar envelope, suggesting that their time-domain waveforms have a similar localized character that does not depend on the repeat period. Because the pumping wavelength is near the edge of our pulse shaper's passband, we used a different method incorporating cross-correlation measurement to investigate the intracavity time-domain waveform (Fig. 4a). Part of the comb power from the drop port was compressed to a short transform-limited pulse train by using a pulse shaper and then used as a sampling signal to test the waveform from the drop port. Figure 4b,c shows the measured cross-correlation results for the 1-FSR and 2-FSR combs. In both cases, the cross-correlation shows a series of dark pulses with

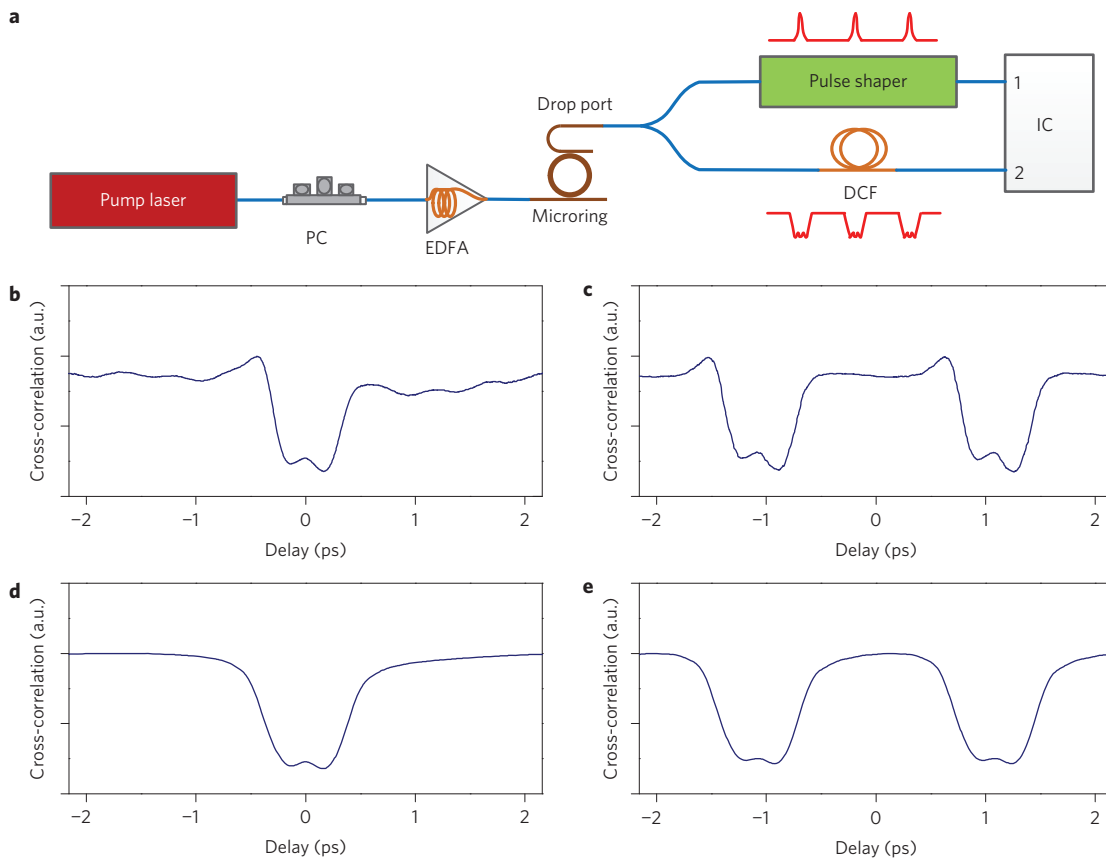


Figure 4 | Self-referenced cross-correlation of the dark pulse combs. **a**, Experimental set-up. PC, polarization controller; EDFA, erbium-doped fibre amplifier; DCF, dispersion-compensating fibre; IC, intensity correlator. **b,c**, Measured cross-correlation for the 1-FSR comb and 2-FSR comb shown in Fig. 3d,III and 3g,III, respectively. The width of the compressed bright pulse after the pulse shaper is ~ 190 fs. **d,e**, Simulated cross-correlation for the 1-FSR (**d**) and 2-FSR (**e**) combs. (See Fig. 5 for simulation details.)

approximately the same shape. The width of the dark pulse is ~ 700 fs. The numerical simulation results based on the estimated experimental parameters are shown in Fig. 4d,e (see Fig. 5 for simulation details). The simulated dark pulse cross-correlation width is ~ 800 fs, which is close to the experimental observation.

The resonance frequency shifts induced by mode interactions are affected by changes in the microresonator operating conditions, such as those associated with the comb transitions described above. This must be included in the simulations that follow in order to capture the salient physics. To provide experimental evidence for this phenomenon, we measured the resonance frequencies for a pumped cavity (for results see Fig. 3b). The laser was pumping mode -7 with 1 W. The red detuning of the pump laser with respect to the cold-cavity resonance was ~ 0.5 nm. A second scanning probe laser was used to measure the microring transmission at the drop port. No combs were generated in this measurement. The resonance jumps of modes 1 and 2 are altered in comparison to the cold cavity, which provides clear evidence of the mode interaction change in a pumped cavity. However, in the case of comb generation, the details of the mode interaction change are very difficult to measure in experiments by scanning the transmission, due to the interference of comb lines and the mixture of the thermal and Kerr effects.

Numerical simulation

The comb generation behaviour can be modelled through numerical simulations using the standard Lugiato–Lefever (L–L) equation^{20,32}, modified to include mode interaction (see Supplementary Section 2 for a discussion of the L–L equation). Figure 5 shows the simulation

results for the microring in Fig. 3a (see Methods for simulation parameters). The intracavity field at the start of simulation is the steady-state c.w. solution on the upper branch of the bistability curve plus weak noise. Figure 5a shows the evolution of the optical spectrum versus slow time when mode 1 is pumped. A 1-FSR comb is generated. The transient images of the comb spectrum and the time-domain waveform are shown in Fig. 5b,c, respectively. The detuning of the pump laser with respect to the cold-cavity resonance is increased at 45 ns after the mode interaction induced initial comb lines grow. The comb then transitions to a breather state that changes periodically over time^{23,25}. This behaviour is similar to that of the experimental result shown in Fig. 3d,I. The measured comb intensity noise contains several narrow peaks, indicating quasi-periodic changing of the comb state. In the simulation, the breather comb transitions to a stable state after the detuning is increased further at 105 ns. The time-domain waveform shows one dark pulse per roundtrip. Figure 5d–f shows the simulation results for the 2-FSR comb when mode 0 is pumped. The detuning is increased at 200 ns in this simulation. The comb then transitions to a stable mode-locked state that is close to the experimental result shown in Fig. 3g,III. The time-domain waveform shows two dark pulses per roundtrip. The excitation behaviour of dark pulses revealed by simulations is similar to our experimental observations. The deviations between simulation and experiment are partially attributed to the dynamic change of mode interactions during the pump tuning process, which are difficult to measure and hence difficult to capture exactly in the simulation. Similar numerical simulations, showing good agreement with our measurements for the microring of Fig. 1a, are shown in Supplementary Section 5.

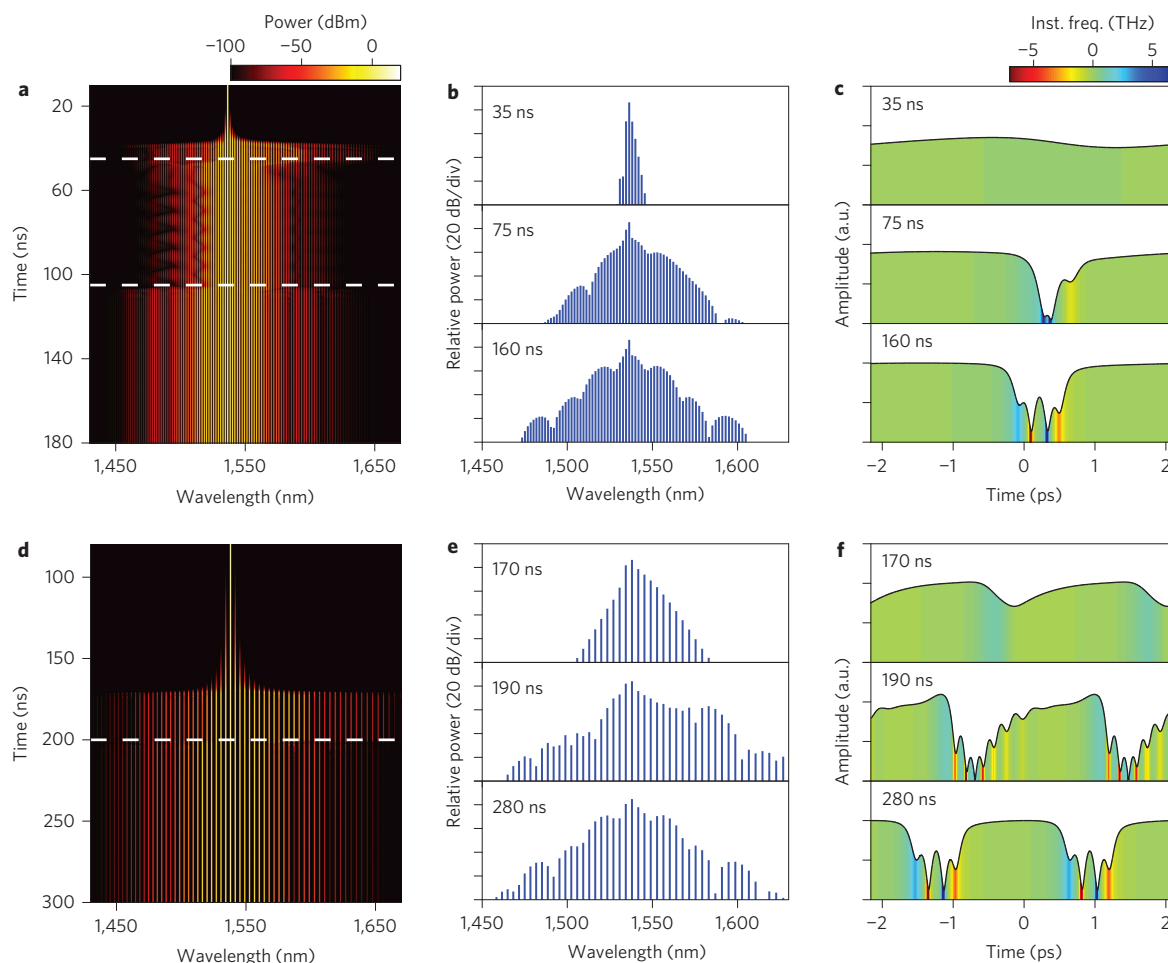


Figure 5 | Simulation of dark pulse excitation for the microring in Fig. 3a. The initial intracavity field is the steady-state upper-branch c.w. solution plus weak noise. The mode interaction is taken into account by applying an additional phase shift to modes 1 and 2. **a**, Evolution of the comb spectrum versus slow time when mode 1 is pumped. The phase detuning is increased at slow times of 45 and 105 ns (white dashed lines). **b,c**, Transient comb spectrum and waveform at different times in **a**. Inst. freq., instantaneous frequency. **d**, Evolution of the comb spectrum versus slow time when mode 0 is pumped. The phase detuning is increased at 200 ns. **e,f**, Transient comb spectrum and waveform at different times in **d**.

Discussion and summary

Further simulation results suggest that the generation of stable dark pulses is related to interaction of fronts that connect the two steady-state solutions of the c.w. bistability curve (Supplementary Section 6). The fronts are formed due to the modulational instability enabled by mode interaction and are usually accompanied by growing of the initial comb lines and wave breaking⁴³. As found in spatial-domain studies of driven nonlinear cavities, when two fronts are close to each other, they may be mutually trapped to generate stable localized structures^{28,29}. We believe this phenomenon may help explain the dark pulses we observe in the time domain. Our dark pulses may also be related to the dark dissipative solitons and platicons discussed in ref. 44. However, the dark pulses demonstrated here differ qualitatively from the topological dark solitons observed in normal-dispersion optical fibres^{45,46}; the π phase shift carried by the background of the fundamental optical-fibre dark soliton is incompatible with the periodic boundary conditions imposed in a cavity. Other operating regimes are also possible, such as the generation of bright pulses recently reported at the output of a SiN microresonator with wavelength-dependent absorption and apparently very weak global normal dispersion⁴⁷.

In summary, we have demonstrated mode-locking transitions as well as dark pulse formation in normal-dispersion microresonators. Such dark pulses in the normal-dispersion regime have a very different nature from bright soliton pulses in the anomalous-dispersion

regime. As well as their great scientific interest, microresonator dark pulses also have their advantages in practical applications. As most nonlinear materials have normal dispersion, tailoring of the microresonator geometry is generally required to achieve overall anomalous dispersion^{5,48,49}. Although such waveguide engineering works well around the telecom band, the ability to mode-lock in the normal-dispersion regime, as reported here, increases the freedom in the microresonator design and may make it possible to generate Kerr combs in an extended wavelength range. This might prove especially important in the visible, where material dispersion is likely to dominate. Furthermore, in the process of dark pulse formation, the pump laser frequency or the microresonator does not need to be tuned at a carefully selected speed to overcome the thermal instability issue as needed for bright soliton formation in the anomalous-dispersion region¹⁷. This may allow reduced system complexity. Another advantage of dark pulse combs demonstrated by our experiments is the excellent repeatability. Similar transition behaviour can be achieved each time the pump laser is tuned into resonance with the same power. The good repeatability of dark pulses is related to the excitation pathway, which is regulated by mode interaction. In comparison, because bright solitons are excited by the broadband chaotic state before the mode-locking transition, the transition exhibits a stochastic behaviour, meaning that different numbers of soliton pulses may be generated under essentially identical experimental conditions¹⁷.

Methods

Methods and any associated references are available in the [online version of the paper](#).

Received 19 January 2015; accepted 3 July 2015;
published online 10 August 2015

References

- Del'Haye, P. *et al.* Optical frequency comb generation from a monolithic microresonator. *Nature* **450**, 1214–1217 (2007).
- Savchenkov, A. A. *et al.* Tunable optical frequency comb with a crystalline whispering gallery mode resonator. *Phys. Rev. Lett.* **101**, 093902 (2008).
- Levy, J. S. *et al.* CMOS-compatible multiple-wavelength oscillator for on-chip optical interconnects. *Nature Photon.* **4**, 37–40 (2010).
- Razzari, L. *et al.* CMOS-compatible integrated optical hyper-parametric oscillator. *Nature Photon.* **4**, 41–45 (2010).
- Savchenkov, A. A. *et al.* Kerr combs with selectable central frequency. *Nature Photon.* **5**, 293–296 (2011).
- Foster, M. A. *et al.* Silicon-based monolithic optical frequency comb source. *Opt. Express* **19**, 14233–14239 (2011).
- Okawachi, Y. *et al.* Octave-spanning frequency comb generation in a silicon nitride chip. *Opt. Lett.* **36**, 3398–3400 (2011).
- Kippenberg, T. J., Holzwarth, R. & Diddams, S. A. Microresonator-based optical frequency combs. *Science* **332**, 555–559 (2011).
- Grudinin, I. S., Baumgartel, L. & Yu, N. Frequency comb from a microresonator with engineered spectrum. *Opt. Express* **20**, 6604–6609 (2012).
- Wang, C. Y. *et al.* Mid-infrared optical frequency combs at 2.5 μm based on crystalline microresonators. *Nature Commun.* **4**, 1345 (2013).
- Ferdous, F. *et al.* Spectral line-by-line pulse shaping of on-chip microresonator frequency combs. *Nature Photon.* **5**, 770–776 (2011).
- Papp, S. B. & Diddams, S. A. Spectral and temporal characterization of a fused-quartz-microresonator optical frequency comb. *Phys. Rev. A* **84**, 053833 (2011).
- Wang, P.-H. *et al.* Observation of correlation between route to formation, coherence, noise, and communication performance of Kerr combs. *Opt. Express* **20**, 29284–29295 (2012).
- Herr, T. *et al.* Universal formation dynamics and noise of Kerr-frequency combs in microresonators. *Nature Photon.* **6**, 480–487 (2012).
- Saha, K. *et al.* Modelocking and femtosecond pulse generation in chip-based frequency combs. *Opt. Express* **21**, 1335–1343 (2013).
- Del'Haye, P., Beha, K., Papp, S. B. & Diddams, S. A. Self-injection locking and phase-locked states in microresonator-based optical frequency combs. *Phys. Rev. Lett.* **112**, 043905 (2014).
- Herr, T. *et al.* Temporal solitons in optical microresonators. *Nature Photon.* **8**, 145–152 (2014).
- Herr, T. *et al.* Mode spectrum and temporal soliton formation in optical microresonators. *Phys. Rev. Lett.* **113**, 123901 (2014).
- Lamont, M. R. E., Okawachi, Y. & Gaeta, A. L. Route to stabilized ultrabroadband microresonator-based frequency combs. *Opt. Lett.* **38**, 3478–3481 (2013).
- Coen, S., Randle, H. G., Sylvestre, T. & Erkintalo, M. Modeling of octave-spanning Kerr frequency combs using a generalized mean-field Lugiato–Lefever model. *Opt. Lett.* **38**, 37–39 (2013).
- Matsko, A. B. *et al.* Mode-locked Kerr frequency combs. *Opt. Lett.* **36**, 2845–2847 (2011).
- Matsko, A. B., Savchenkov, A. A., Ilchenko, V. S., Seidel, D. & Maleki, L. Hard and soft excitation regimes of Kerr frequency combs. *Phys. Rev. A* **85**, 023830 (2012).
- Matsko, A. B., Savchenkov, A. A. & Maleki, L. On excitation of breather solitons in an optical microresonator. *Opt. Lett.* **37**, 4856–4858 (2012).
- Matsko, A. B., Savchenkov, A. A. & Maleki, L. Normal group-velocity dispersion Kerr frequency comb. *Opt. Lett.* **37**, 43–45 (2012).
- Godey, C., Balakireva, I. V., Coillet, A. & Chembo, Y. K. Stability analysis of the spatiotemporal Lugiato–Lefever model for Kerr optical frequency combs in the anomalous and normal dispersion regimes. *Phys. Rev. A* **89**, 063814 (2014).
- Ippen, E. P. Principles of passive mode locking. *Appl. Phys. B* **58**, 159–170 (1994).
- Haus, H. A. Mode-locking of lasers. *IEEE J. Sel. Top. Quantum Electron.* **6**, 1173–1185 (2000).
- Rosanon, N. N. *Spatial Hysteresis and Optical Patterns* (Springer, 2002).
- Boardman, A. D. & Sukhorukov, A. P. *Soliton-driven Photonics* (Springer, 2001).
- Leo, F. *et al.* Temporal cavity solitons in one-dimensional Kerr media as bits in an all-optical buffer. *Nature Photon.* **4**, 471–476 (2010).
- Carmon, T., Yang, L. & Vahala, K. J. Dynamical thermal behavior and thermal self-stability of microcavities. *Opt. Express* **12**, 4742–4750 (2004).
- Haelterman, M., Trillo, S. & Wabnitz, S. Dissipative modulation instability in a nonlinear dispersive ring cavity. *Opt. Commun.* **91**, 401–407 (1992).
- Coen, S. & Haelterman, M. Modulational instability induced by cavity boundary conditions in a normally dispersive optical fiber. *Phys. Rev. Lett.* **79**, 4139–4142 (1997).
- Hansson, T., Modotto, D. & Wabnitz, S. Dynamics of the modulational instability in microresonator frequency combs. *Phys. Rev. A* **88**, 023819 (2013).
- Coen, S. *et al.* Bistable switching induced by modulational instability in a normally dispersive all-fibre ring cavity. *J. Opt. B* **1**, 36–42 (1999).
- Coillet, A. *et al.* Azimuthal Turing patterns, bright and dark cavity solitons in Kerr combs generated with whispering-gallery-mode resonators. *IEEE Photon. J.* **5**, 6100409 (2013).
- Liang, W. *et al.* Generation of a coherent near-infrared Kerr frequency comb in a monolithic microresonator with normal GVD. *Opt. Lett.* **39**, 2920–2923 (2014).
- Del'Haye, P., Arcizet, O., Gorodetsky, M. L., Holzwarth, R. & Kippenberg, T. J. Frequency comb assisted diode laser spectroscopy for measurement of microcavity dispersion. *Nature Photon.* **3**, 529–533 (2009).
- Savchenkov, A. A. *et al.* Kerr frequency comb generation in overmoded resonators. *Opt. Express* **20**, 27290–27298 (2012).
- Liu, Y. *et al.* Investigation of mode coupling in normal-dispersion silicon nitride microresonators for Kerr frequency comb generation. *Optica* **1**, 137–144 (2014).
- Ramelow, S. *et al.* Strong polarization mode coupling in microresonators. *Opt. Lett.* **39**, 5134–5137 (2014).
- Wang, P.-H. *et al.* Drop-port study of microresonator frequency combs: power transfer, spectra and time-domain characterization. *Opt. Express* **21**, 22441–22452 (2013).
- Malaguti, S., Bellanca, G. & Trillo, S. Dispersive wave-breaking in coherently driven passive cavities. *Opt. Lett.* **39**, 2475–2478 (2014).
- Lobanov, V. E., Lihachev, G., Kippenberg, T. J. & Gorodetsky, M. L. Frequency combs and platons in optical microresonators with normal GVD. *Opt. Express* **23**, 7713–7721 (2015).
- Weiner, A. M. *et al.* Experimental observation of the fundamental dark soliton in optical fibers. *Phys. Rev. Lett.* **61**, 2445–2448 (1988).
- Hasegawa, A. & Matsumoto, M. *Optical Solitons in Fibers* (Springer, 2003).
- Huang, S.-W. *et al.* Mode-locked ultrashort pulse generation from on-chip normal dispersion microresonators. *Phys. Rev. Lett.* **114**, 053901 (2015).
- Riemensberger, J. *et al.* Dispersion engineering of thick high-Q silicon nitride ring-resonators via atomic layer deposition. *Opt. Express* **20**, 27661–27669 (2012).
- Zhang, L. *et al.* Intra-cavity dispersion of microresonators and its engineering for octave-spanning Kerr frequency comb generation. *IEEE J. Sel. Top. Quantum Electron.* **20**, 5900207 (2014).

Acknowledgements

This work was supported in part by the National Science Foundation under grants ECCS-1102110 and ECCS-1126314, by the Air Force Office of Scientific Research under grant FA9550-12-1-0236 and by the DARPA PULSE program through grant W31P40-13-1-0018 under AMRDEC. The authors thank C.R. Menyuk and G. D'Aguanno for discussions and the reviewers for their comments.

Author contributions

X.X. led the experiments, with assistance from Y.L., P.H.W., S.C., J.W. and D.E.L. X.X. analysed the data and performed the numerical simulations. X.X. and Y.X. designed the SiN microring layout with assistance from P.H.W. and J.W. Y.X. fabricated the microring. X.X. and A.M.W. wrote the manuscript. The project was organized and coordinated by A.M.W. and M.Q.

Additional information

Supplementary information is available in the [online version](#) of the paper. Reprints and permissions information is available online at www.nature.com/reprints. Correspondence and requests for materials should be addressed to A.M.W.

Competing financial interests

The authors declare no competing financial interests.

Methods

Comb generation with thermal tuning. The radius of the SiN microring shown in Fig. 1a is 100 μm, and the dimensions of the microring waveguide cross-section are 2 μm × 550 nm. The resistance of the microheater is 291 Ω. By changing the voltage applied to the microheater (thus changing the heating power), the mode used for comb generation can be tuned with an efficiency of 0.82 nm W⁻¹. The thermal tuning efficiency of the second mode family, which is not pumped for comb generation, is 0.79 nm W⁻¹. For the comb generation in Fig. 1d the pump laser wavelength was fixed at 1,549.3 nm, which was initially to the red of the resonance used (~1,548.4 nm) when the heater power was zero, and the pump power was ~1.7 W (off-chip power; coupling loss per facet of ~3 dB). The heater voltage was first increased to 20 V (the corresponding resonance was redshifted to ~1,549.5 nm, which was now to the red of the pump) and then slowly reduced to shift the resonance back towards the pump. When the heater voltage was 7.95 V, there were two primary comb lines far away (54-FSR) from the pump and also some secondary comb lines with 1-FSR spacing (Fig. 1d,I). The comb at this stage showed broadband intensity noise accompanied by some peaks (Fig. 1e,I). When the heater voltage was further reduced to 7.73 V, a sudden transition to a broadband comb was observed (Fig. 1d,II), still with intensity noise, but now appearing as a narrow noise peak around 700 MHz (Fig. 1e,II). When the heater voltage was further reduced to 7.34 V, the comb spectrum remained similar (Fig. 1d,III), while the intensity noise dropped below the background noise of the radiofrequency spectrum analyser (Fig. 1e,III).

Line-by-line comb shaping. The method of line-by-line phase compensation to form a transform-limited pulse is the same as that described in ref. 11. The use of this method to determine the spectral phase of the as-generated waveform has been reported in a number of previous studies and its validity has been confirmed by direct comparison to independent measurement methods^{50,51}. In probing the spectral phases shown in Fig. 2d, the state of the pulse shaper was updated by repeating the line-by-line phase compensation procedure only when a noticeable increase of the autocorrelation background was observed after the comb was tuned to the next wavelength. Figure 2d shows five independent phase measurements from line-by-line compensation runs at 1,549.0, 1,549.5, 1,549.7, 1,549.8 and 1,550.0 nm, as well as an additional run (1,549.3 nm) repeated on another day.

Autocorrelation and cross-correlation. The intensity correlation was measured by detecting the second harmonic generation signal through a β-barium borate crystal. A switchable mirror was used to select the two optical inputs to make the set-up work in autocorrelation measuring mode or cross-correlation measuring mode. An erbium-doped fibre amplifier (EDFA) was used after the pulse shaper to compensate the link loss (not shown in Figs 1c, 4a). In the autocorrelation measurement (Fig. 1c), a length of dispersion-compensating fibre (DCF) was used to roughly compensate the dispersion of the fibre link between the output port of the microring chip and the input ports of the correlator. The residual second-order dispersion (group velocity dispersion) as well as higher-order dispersion were measured by injecting ~180 fs pulses from a mode-locked fibre laser into the fibre link and were further compensated by programming the pulse shaper. In the cross-correlation measurement (Fig. 4a), the fibre length between the output port of the microring chip and input port 2 of the correlator was much shorter than that in the autocorrelation measurement because there was no pulse shaper and EDFA in this path. The dispersion was then compensated by just using a short length of DCF.

Numerical simulation. The standard L–L equation^{20,32}, written as

$$t_R \frac{\partial E(t, \tau)}{\partial t} = \left[-\alpha - i\delta_0 - iL \frac{\beta_2}{2} \frac{\partial^2}{\partial \tau^2} + iyL|E(t, \tau)|^2 \right] E(t, \tau) + \sqrt{\theta} E_{in}$$

can be used to model the comb generation behaviour by taking into account the mode-interaction-induced phase shift to the comb lines. For the simulation results shown in Fig. 5, the roundtrip cavity loss $\alpha = 3.10 \times 10^{-3}$ and the bus waveguide coupling coefficient $\theta = 1.93 \times 10^{-3}$ are extracted by measuring the resonance width and the coupling condition (Supplementary Section 4.4). The estimated nonlinear

coefficient is $\gamma = n_2 \omega_0 / (c A_{eff}) \approx 0.89 \text{ m}^{-1} \text{ W}^{-1}$, where the nonlinear refractive index is $n_2 = 2.4 \times 10^{-19} \text{ m}^2 \text{ W}^{-1}$, the resonance frequency $\omega_0 = 2\pi \times 1.95 \text{ THz}$, c is the speed of light in vacuum, and the effective mode area A_{eff} is $\sim 1.10 \mu\text{m}^2$. The other parameters are the roundtrip time $t_R = 4.32 \text{ ps}$, the roundtrip length $L = 2\pi \times 100 \mu\text{m}$ and the second-order dispersion coefficient $\beta_2 = 186.9 \text{ ps}^2 \text{ km}^{-1}$. The initial intracavity field is the steady-state c.w. solution on the upper branch of the bistability curve plus weak noise (~1 pW per mode). The mode interaction is taken into account by applying additional phase shifts to modes 1 and 2 in the frequency-domain step of the split-step Fourier routine. The additional phase shift per roundtrip $\Delta\phi$ and the corresponding resonance shift Δf are related by $\Delta\phi = -2\pi\Delta f/\text{FSR}$. The resonance shifts of modes 1 and 2 in simulation are roughly of the same order as those obtained in measurements (Fig. 3b). For the 1-FSR comb simulation, mode 1 is pumped with 0.4 W. The initial phase detuning of the pump laser with respect to the cold cavity is $\delta_0 = 1.2 \times 10^{-2} \text{ rad}$ at the beginning of the simulation, and the mode-interaction-induced resonance shifts of modes 1 and 2 are -130 and 230 MHz, respectively. After the initial comb lines are generated, the pump phase detuning is increased to $1.4 \times 10^{-2} \text{ rad}$ at a slow time of 45 ns. To simulate the dynamic change of mode interaction with detuning, the resonance shifts of modes 1 and 2 are changed to -100 and 100 MHz, respectively. The comb then transitions to a breather state that is similar to the experimental result in Fig. 3d,I. The pump detuning is increased further to $1.85 \times 10^{-2} \text{ rad}$ at a slow time of 105 ns and the resonance shifts of modes 1 and 2 are changed to -80 and 50 MHz, respectively. The comb transitions to a stable mode-locked state that is close to the experimental result in Fig. 3d,III. For the 2-FSR comb simulation, mode 0 is pumped with 0.3 W. The initial pump detuning is $1.95 \times 10^{-2} \text{ rad}$ and the resonance shifts of modes 1 and 2 are -130 and 230 MHz, respectively. The pump detuning is increased to $2.15 \times 10^{-2} \text{ rad}$ at 200 ns and the resonance shifts of modes 1 and 2 are changed to -80 and 50 MHz, respectively. A stable mode-locked 2-FSR comb is obtained that is similar to the experimental result in Fig. 3g,III.

Please note that the L–L equation generally uses an $\exp(-i\omega t)$ convention^{20,32}, a convention that we adopt also in our simulations. However, for our experimental measurements we use the $\exp(i\omega t)$ convention prevalent in ultrafast optics⁵². Therefore, in comparing simulation with experiment, one must take into account the opposite sign conventions. In the present Article we choose to plot all the spectral phases using the $\exp(i\omega t)$ convention. In particular, in the ultrafast optics convention we have

$$e(t) = \text{Re}(a(t)e^{i\omega_0 t}) = \frac{1}{2} [a(t)e^{i\omega_0 t} + a^*(t)e^{-i\omega_0 t}] = \frac{1}{2} [|a(t)|e^{i(\omega_0 t + \phi(t))} + |a(t)|e^{-i(\omega_0 t + \phi(t))}]$$

and in the convention used for the L–L equation we have

$$e(t) = \text{Re}(a(t)e^{-i\omega_0 t}) = \frac{1}{2} [a(t)e^{-i\omega_0 t} + a^*(t)e^{i\omega_0 t}] = \frac{1}{2} [|a(t)|e^{-i(\omega_0 t - \phi(t))} + |a(t)|e^{i(\omega_0 t - \phi(t))}]$$

In both expressions above we are using $a(t)$ as the complex envelope function, with t representing fast time, a terminology common in ultrafast optics⁵². So if we obtain $\phi(t)$ from the L–L equation, we need to change it to $-\phi(t)$ if we wish to compare it to experimental data that we plot using the prevalent ultrafast optics convention. Equivalently we can say if we have $a(t)$ from the L–L equation, we need to change it to $a^*(t)$ if we want to be consistent with the ultrafast optics convention.

References

50. Miao, H., Leaird, D. E., Langrock, C., Fejer, M. M. & Weiner, A. M. Optical arbitrary waveform characterization via dual-quadrature spectral shearing interferometry. *Opt. Express* **17**, 3381–3389 (2009).
51. Del’Haye, P. *et al.* Phase steps and resonator detuning measurements in microresonator frequency combs. *Nature Commun.* **6**, 5668 (2015).
52. Weiner, A. M. *Ultrafast Optics* (Wiley, 2009).